

## RESEARCH ARTICLE

10.1002/2017JC013580

## Mechanisms of the 40–70 Day Variability in the Yucatan Channel Volume Transport

## Key Points:

- The volume transport in the Yucatan Channel displays a 40–70 day variability
- This variability is regulated by upstream regions, i.e., the North Brazil Current
- The 40–70 day variability is caused by intrinsic ocean processes

## Correspondence to:

R. M. van Westen,  
r.m.vanwesten@uu.nl

## Citation:










van Westen, R. M., Dijkstra, H. A., Klees, R., Riva, R. E. M., Cornelis Slobbe, D., van der Boog, C. G., . . . Bouma, T. J. (2018). Mechanisms of the 40–70 day variability in the Yucatan Channel volume transport. *Journal of Geophysical Research: Oceans*, 123, 1286–1300. <https://doi.org/10.1002/2017JC013580>

Received 26 OCT 2017

Accepted 31 JAN 2018

Accepted article online 5 FEB 2018

Published online 16 FEB 2018

René M. van Westen<sup>1</sup> , Henk A. Dijkstra<sup>1</sup> , Roland Klees<sup>2</sup> , Riccardo E. M. Riva<sup>2</sup> , D. Cornelis Slobbe<sup>2</sup> , Carine G. van der Boog<sup>2</sup>, Caroline A. Katsman<sup>2</sup> , Adam S. Candy<sup>2</sup> , Julie D. Pietrzak<sup>2</sup>, Marcel Zijlema<sup>2</sup>, Rebecca K. James<sup>3</sup> , and Tjeerd J. Bouma<sup>3</sup> 

<sup>1</sup>Institute for Marine and Atmospheric Research Utrecht, Department of Physics and Astronomy, Utrecht University, Utrecht, The Netherlands, <sup>2</sup>Environmental Fluid Mechanics Section, Department of Hydraulic Engineering, Civil Engineering and Geosciences, Delft University of Technology, Delft, The Netherlands, <sup>3</sup>Royal Netherlands Institute for Sea Research, Department of Estuarine and Delta Systems, and Utrecht University, Yerseke, The Netherlands

**Abstract** The Yucatan Channel connects the Caribbean Sea with the Gulf of Mexico and is the main outflow region of the Caribbean Sea. Moorings in the Yucatan Channel show high-frequency variability in kinetic energy (50–100 days) and transport (20–40 days), but the physical mechanisms controlling this variability are poorly understood. In this study, we show that the short-term variability in the Yucatan Channel transport has an upstream origin and arises from processes in the North Brazil Current. To establish this connection, we use data from altimetry and model output from several high-resolution global models. A significant 40–70 day variability is found in the sea surface height in the North Brazil Current retroflection region with a propagation toward the Lesser Antilles. The frequency of variability is generated by intrinsic processes associated with the shedding of eddies, rather than by atmospheric forcing. This sea surface height variability is able to pass the Lesser Antilles, it propagates westward with the background ocean flow in the Caribbean Sea and finally affects the variability in the Yucatan Channel volume transport.

## 1. Introduction

From observations and model studies, the mean volume transport of the Yucatan Channel (YC), connecting the Caribbean Sea with the Gulf of Mexico, is about 16–34 sverdrup ( $1 \text{ Sv} \equiv 10^6 \text{ m}^3 \text{ s}^{-1}$ ; Alvera-Azcarate et al., 2009; Candela et al., 2003; Ezer et al., 2003; Johns et al., 2002; Ochoa et al., 2001; Schmitz & Richardson, 1991; Sheinbaum et al., 2002). Upstream eddies can be advected through the YC and affect the variability in the YC (Abascal et al., 2003). This variability can be carried downstream along the characteristic background current and may influence downstream regions, such as the Loop Current in the Gulf of Mexico. For example, it has been suggested that variability in the deep return YC transport flow is related to the shedding of rings by the Loop Current (Ezer et al., 2003; Oey, 2004). Moorings of the YC transport show a variability of about 40 days (Abascal et al., 2003; Bunge et al., 2002), but observational records are short and sparse (Abascal et al., 2003; Bunge et al., 2002; Candela et al., 2003; Sheinbaum et al., 2002).

From model studies, the variability of the velocity fields in the YC was studied through empirical orthogonal function (EOF) analysis in Ezer et al. (2003). It was shown that the power spectra of the first four principle components (PCs) have peaks at low frequencies ( $>170$  days), but also a 40–60 day variability was found. Abascal et al. (2003) suggest that the variability in the YC is regulated by (upstream) eddies, generated by intrinsic variability or atmospheric forcing in the Caribbean Sea. Modeling studies (Jouanno et al., 2009) indeed show that baroclinic instability can occur almost everywhere in the Caribbean basin. Topographic ridges can also interact with Caribbean eddies and affect the monthly-to-seasonal circulation variability of the Caribbean Sea (Lin et al., 2012; Molinari et al., 1981). A more recent study by Jouanno and Sheinbaum (2013) demonstrates the substantial influence of intense wind stress anomalies on the formation of eddies.

On the other hand, there is evidence that anticyclonic rings from the North Brazil Current (NBC) retroflection influence the variability in the Caribbean Sea. These so-called NBC rings, having diameters up to 400 km, are shed near 8°N (Condie, 1991; Csanady, 1985; Fratantoni & Glickson, 2002) in the tropical Atlantic Ocean and are advected northwestward along with the background ocean flow toward the Lesser Antilles. Earlier studies, based on in situ data (Johns et al., 1990) and Fratantoni et al. (1995), estimated a ring-shedding

**Table 1**  
Overview of the Four Data Sets

Data set	Years	Total length (days to weeks)	Horizontal resolution	Velocity field (m)	Depth levels
AVISO	1993–2014	8,035–1,147	0.25° × 0.25°	Surface	1
Mercator	2007–2016	3,653–521	1/12° × 1/12°	0.5–5,500	50
POP	266–269	1,460–208	0.4° × 0.4°	5–15	2
CESM	201–204	1,460–208	0.4° × 0.4°	5–5,875	42

Note. The analyzed (model) years, the total length (days and weeks) of the data set, horizontal resolution, the depth range of the horizontal velocity fields, and the total number of depth levels. The raw data/model output is provided as daily averaged fields.

frequency of two to four events per year. Later studies (Fratantoni & Glickson, 2002; Goni & Johns, 2001; Johns et al., 2003) suggest the formation of about five to nine rings per year. The rings may account for 1/3 of the interhemispheric mass transport in the Atlantic Meridional Overturning Circulation (AMOC; Goni & Johns, 2001), or  $1.0 \pm 0.4$  Sv per ring (Fratantoni & Glickson, 2002).

Many of the NBC rings propagate northwestward and are deflected by the island barrier at the eastern entrance of the Caribbean Sea. However, modeling studies (Carton & Chao, 1999; Murphy et al., 1999; Simmons & Nof, 2002), drifter studies (Fratantoni & Richardson, 2006; Richardson, 2005), altimetry observations (Goni & Johns, 2001), and freshwater plumes studies (Chérubin & Richardson, 2007) provide indications for the advection of ring filaments through the Caribbean

island chain. Jouanno et al. (2009) suggest that the eddy variability in the Caribbean Sea is influenced by filaments of the NBC rings.

In this study, we aim to answer the question whether there is an upstream influence on the YC volume transport variability originating from the NBC retroflexion. In section 2, the data sets which are analyzed are presented and in section 3, we provide an overview of the methods used. In section 4, the position of the NBC retroflexion and the frequency of the ring-shedding events are studied. In addition, it is investigated if (filaments of the) NBC rings are able to pass the Lesser Antilles. In section 5, the influence of NBC rings on the sea surface height variability in the Caribbean Sea is analyzed and in particular whether this variability reaches the YC and affects the YC transport. The results are summarized and discussed in section 6.

## 2. Observations and Model Output

An overview of the data sets used in this study is shown in Table 1.

We use 22 years (1993–2014) of altimetry data (DUACS DT2014) from the Archiving, Validation and Interpretation of Satellite Oceanographic data base (AVISO, <http://www.aviso.altimetry.fr/en/data.html>). The observational data set is composed of daily averaged gridded horizontal geostrophic velocities, sea surface height (SSH) relative to the geoid, and sea level anomalies (SLA). The provided horizontal grid resolution is  $0.25^\circ \times 0.25^\circ$ . However, the actual temporal and spatial resolution are coarser (10 days and  $1^\circ$ ) due to differences in revisit time and crossover trajectories of the satellites (Le Bars et al., 2014). Although the gridded AVISO data set is convenient to work with, it has some drawbacks in the interpretation of the results, as the fields are strongly interpolated and filtered (Castelão & Johns, 2011).

In Figure 1a, the time mean geostrophic velocity, as deduced from the AVISO data, is shown over the region of interest. Strong surface velocities appear near the NBC and north of the YC. Also the mean westward current (i.e., the Caribbean Current) from the Lesser Antilles through the Caribbean Sea to the YC is clearly

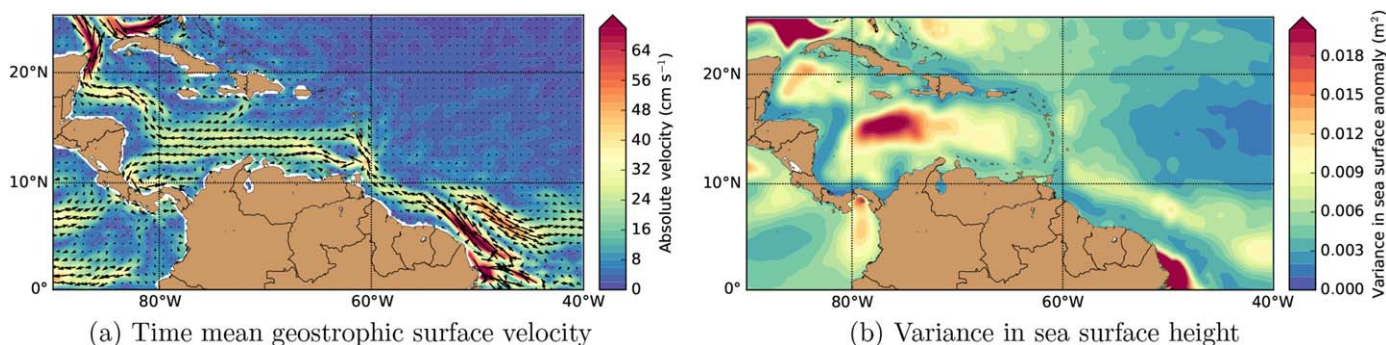


**Figure 1.** (a) Time mean geostrophic surface velocity (quiver) and absolute values (shading). (b) Variance in sea surface height. The analyzed period is 22 years (1993–2014) of daily averaged fields by the AVISO data set.

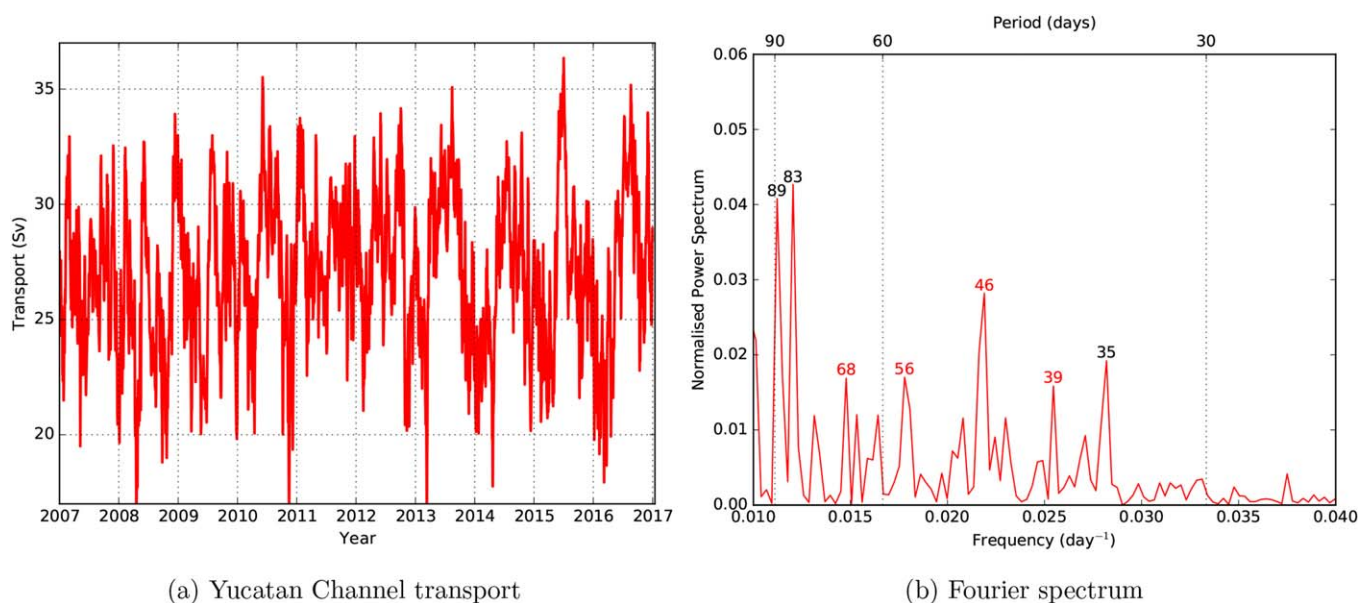


**Figure 2.** (a) Volume transport in the Yucatan Channel over 10 years (2007–2016) of daily output of the Mercator data set. (b) Fourier spectrum of the band-pass filtered (30–120 days) Yucatan Channel volume transport time series. The periods (in days) for specific peaks are indicated. The periods marked in red are significant at the 95% confidence interval (see Table 8).

seen, with speeds of about  $0.3 \text{ m s}^{-1}$ . The variance of SSH, shown in Figure 1b, indicates that the dominant variability is located near the Amazon outflow, the central Caribbean Sea and the YC.

We also use 10 years (2007–2016) of model output from the Operational Mercator global ocean analysis at  $1/12^\circ$  data assimilation set (<http://marine.copernicus.eu/services-portfolio/access-to-products/>). Mercator uses the NEMO ocean model (Madec, 2008) version 3. Through data assimilation (for further details we refer to the detailed description of Mercator provided by Copernicus-Marine environment monitoring service), Mercator is “steered” toward (a limited set of) observations. Note that Mercator also assimilates altimetry from AVISO, but Mercator provides a higher spatial resolution of SSH fields and additional quantities, such as horizontal velocities, temperature, and salinity fields. Moreover, the model output comprises daily averaged fields and is available at 50 nonequidistant depth layers between 0.5 and 5,500 m, where the vertical resolution decreases with increasing depth. The YC transport time series from these output (Figure 2a) displays a strong annual cycle that dominates the power spectrum. When the time series is filtered by a band-pass filter of 30–120 days before making the Fourier spectrum, several peaks arise (Figure 2b); we will show in section 5 below that the variability in the range of 40–70 days is significant.

In addition to the AVISO altimetry data set and the Mercator output, we use 4 years of model output from the Parallel Ocean Program (POP; Smith et al., 2010), a state-of-the-art ocean-only model which captures the development and interaction of mesoscale eddies (Hallberg, 2013). The model has a high resolution of  $0.1^\circ$  on a curvilinear grid which is transformed back onto a rectangular grid with grid sizes of about  $0.4^\circ \times 0.4^\circ$ . The model is forced by a yearly repeated seasonal mean and we use the output from equilibrated flows of the 300 year global simulation as described in Weijer et al. (2012) and Le Bars et al. (2016). Using the POP model results and those of the Community Earth System Model (CESM, discussed below) gives the advantage that the role of intrinsic variability can be studied. For example, the variability generated by intense wind stress anomalies (Jouanno & Sheinbaum, 2013) is not represented in POP but it is in CESM. The data set contains daily averaged temperatures, salinities, SSHs and horizontal velocity fields. The model output for daily averaged fields is only available at two depth layers, 5 and 15 m. The model output is analyzed over model years 266–269, over which the upper ocean is in equilibrium.

Finally, we use 4 years of model output from a 210 year simulation of an eddy version of the CESM (Smith et al., 2010; Hurrell et al., 2013). In this simulation, the horizontal resolution of the ocean component (the POP) and sea-ice component are resolved at  $0.1^\circ$ , and atmosphere and land surface at  $0.5^\circ$ . The forcing conditions, such as  $\text{CO}_2$  and aerosols, are the observed ones over the year 2000. The atmosphere and upper

ocean (700 m) are in near equilibrium over the last 50 years of the simulation (see van Westen & Dijkstra, 2017, supporting information). The model output comprises daily averaged temperatures, salinities, SSHs, and horizontal velocity fields (similar to the POP data set). The daily averaged horizontal velocities are available at 42 nonequidistant depth layers between 5 and 5,875 m. The model output is analyzed over model years 201–204, over which the daily averaged velocity fields are available and the upper ocean is in equilibrium during these model years.

### 3. Methods

#### 3.1. Multichannel Singular Spectrum Analysis

The multichannel singular spectrum analysis (M-SSA; Ghil et al., 2002) tool is used to study spatial-temporal variations in SSH and velocity fields and is able to detect (significant) oscillations with red noise as a null-hypothesis (Allen & Smith, 1996). Suppose a time series of the analyzed field (SSH or velocity) has a total length of  $N$  units of time. Each individual time series is decomposed and shifted up to  $M$  time steps, creating  $M$  lagged time series, each with a total length of  $N' = N - M + 1$ . M-SSA analyses the interrelationship of all these lagged time series (Plaut & Vautard, 1994). To assess the significance of the detected oscillations in M-SSA, a Monte Carlo test is implemented (Allen & Robertson, 1996; Allen & Smith, 1996). All the confidence intervals are derived from 2,500 realizations in the Monte Carlo test. After performing the M-SSA, it is possible to find pairs of space-time principal components (ST-PCs) which are associated with a certain (significant) oscillation. These ST-PCs pairs are used to determine the reconstructed components (RCs). The RCs display the spatial-temporal variability for a certain oscillation instead of the full spectrum (e.g., Schmeits & Dijkstra, 2000).

Before applying M-SSA, the time series needs to be prefiltered to detect relevant oscillations. During the prefiltering process, first a linear trend is removed over the analyzed period. Next, seasonality is removed by subtracting the seasonal mean and, optionally, any low-pass or high-pass filter is applied to remove dominant oscillations. If stated, we applied a Butterworth filter. Finally, each time series is normalized (by the standard deviation) afterward. After the prefiltering of the time series, a principal component analysis (PCA) is applied to reduce dimensions. We use the principal components (PCs) which together contain at least 90% of the total variance of all the time series (Schmeits & Dijkstra, 2000). For more (technical) details on M-SSA and its applications, we refer to Vautard and Ghil (1989) and Ghil et al. (2002). A special case of M-SSA is singular spectrum analysis (SSA), where only a single time series is analyzed.

#### 3.2. NBC Retroreflection and Ring-Shedding Events

The NBC closely follows the continental shelf and is moving northwestward. For convenience, the coordinate system is rotated clockwise by  $31^\circ$  (affine transformation), so the new zonal axis represents the continental shelf and is inclined clockwise by  $121^\circ$  from the geographical north (Figure 3a). In this new reference frame, the NBC is more zonal and easier to distinguish in the highly variable ocean flow. The horizontal velocity field (closest to the surface) is projected onto this tilted coordinate system, resulting in a new zonal velocity ( $u_*$ ) and meridional velocity ( $v_*$ ).

In AVISO, the outflow region of the Amazon is omitted due to the high variability of all relevant quantities in time (cf., Figure 1). The magnitude of the derived geostrophic velocities by AVISO is unrealistic large in this region which complicates the detection of the NBC. The horizontal velocity fields which are resolved by the three models do not show unrealistic large values in the Amazon outflow region. Therefore, the Amazon outflow region is not omitted for the models.

To detect the NBC retroreflection, we follow the method described by Cetina-Heredia et al. (2014), with some adjustments. First, the position of the NBC is determined along a random placed meridional cross-section southeastward of the retroreflection. The NBC is defined where the zonal velocity ( $u_*$ ) has the largest magnitude in westward movement along the meridional cross section (see Figure 3b, point A). The flow structure of the NBC can be followed by the SSH isoline that passes through point A. (Sometimes, this SSH isoline fails to capture the NBC retroreflection phenomenon, for example due to distortions before/after a ring-shedding event. In this case, multiple SSH isolines are analyzed to track the retroreflection.) The NBC retroreflection is anticyclonic and the SSH increases in the positive direction of the rotated meridional coordinate. Therefore, the deduced SSH level in point A is set as lower boundary while plotting multiple SSH isolines (each spaced by 0.5 cm). Only the isolines that intersect the meridional cross section at least twice are taken into account.



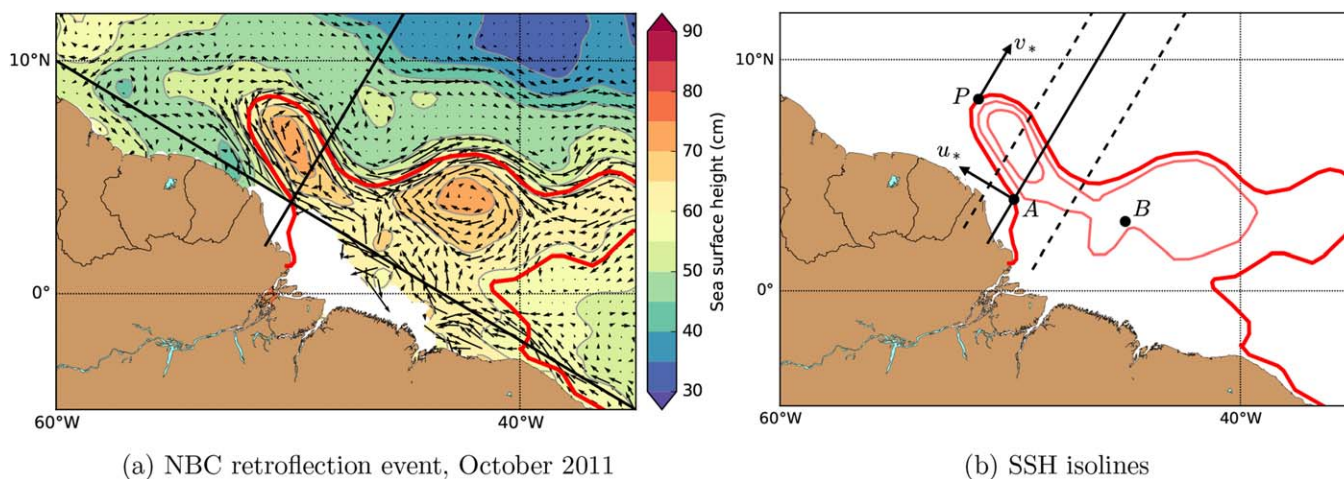


**Figure 3.** (a) Monthly mean observation-derived geostrophic velocity (quiver) and SSH (shading) field in October 2011 of the AVISO data set. The black lines indicate the 31° clockwise rotated coordinate system; the red line is an SSH isoline. (b) Same red SSH isoline and two additional SSH isolines. The dashed meridional lines are the two other cross sections. The NBC is identified to point A including the zonal velocity ( $u_*$ ) of maximum westward movement. The retroflection is determined to occur at point P (51.8°W, 8.2°N) along the SSH isoline, including the meridional velocity ( $v_*$ ) of the retroflection point. The retroflection distance is determined as the distance between point B (45°W, 3°N) and point P.

Each SSH isoline is followed clockwise and an eastward turning of an isoline could be a signature of the NBC retroflection (Cetina-Heredia et al., 2014). We defined the retroflection point when an isoline turns 31° clockwise from the geographical north (parallel to the meridional cross section). The results were not significantly influenced by the threshold of 31° which has been investigated by slightly changing this value by  $\pm 15^\circ$ . During boreal spring, the NBC retroflection region is highly variable, which results in a false detection of the retroflection. Therefore, an additional threshold ( $v_* > v_{crit}$ ) is applied to the meridional velocity of the retroflection point, which was set to  $v_{crit} = 0.2 \text{ m s}^{-1}$ .

The NBC retroflection has a seasonal signature, resulting in varying position in time. In addition, ring-shedding events lead to a temporal northwestward excursion of the retroflection. It is possible that the retroflection is not found while using the meridional cross section as in Figure 3a, while in fact the NBC retroflection is present. Therefore, we placed two other meridional cross sections and conducted the same procedure. If all three cross sections fail to capture the retroflection, it is assumed that no (or weak) retroflection is present and that the region is highly variable.

Ring-shedding events are characterized by a (sudden) southeastward retraction of the NBC retroflection (Frantoni & Glickson, 2002). It is possible to study the retraction of the NBC retroflection in both the longitude and latitude time series of the retroflection position (Dencausse et al., 2010). However, it is more convenient to convert the retroflection position to a scalar by determining the distance between a specified point B (see Figure 3b) and the point P. In the retroflection distance time series, ring-shedding events can be detected by a decrease in distance in the order of a few hundred kilometers over a short period (1–2 weeks).

**Table 2**

*Total Number of Weeks of an Absent or Relatively Weak Retroflection, Including the Seasonal Variation*

Data set	Total	DJF (%)	MAM (%)	JJA (%)	SON (%)
AVISO	139	10.1	59.7	23.0	7.2
Mercator	94	5.3	60.6	30.9	3.2
POP	32	21.9	56.3	18.7	3.1
CESM	42	14.3	54.8	21.4	9.5

*Note.* The retroflection position is determined from all available weekly averaged SSH and horizontal velocity fields for AVISO, Mercator, POP, and CESM.

## 4. Results: North Brazil Current Analysis

In this section, the NBC retroflection (position and seasonality) is analyzed and how SSH variability propagates from the NBC retroflection toward the Caribbean Sea.

### 4.1. Position of Retroflection

The retroflection position is first determined over all the available weeks for each data sets (cf., Table 1). The retroflection is least abundant during boreal spring (see Table 2) in all data sets. The average retroflection position over all the available weekly averaged fields is 51.1°W; 7.9°N (AVISO), 51.0°W; 8.3°N (Mercator), 50.3°W; 7.3°N (POP), and 50.5°W; 7.8°N (CESM). The average retroflection position shows

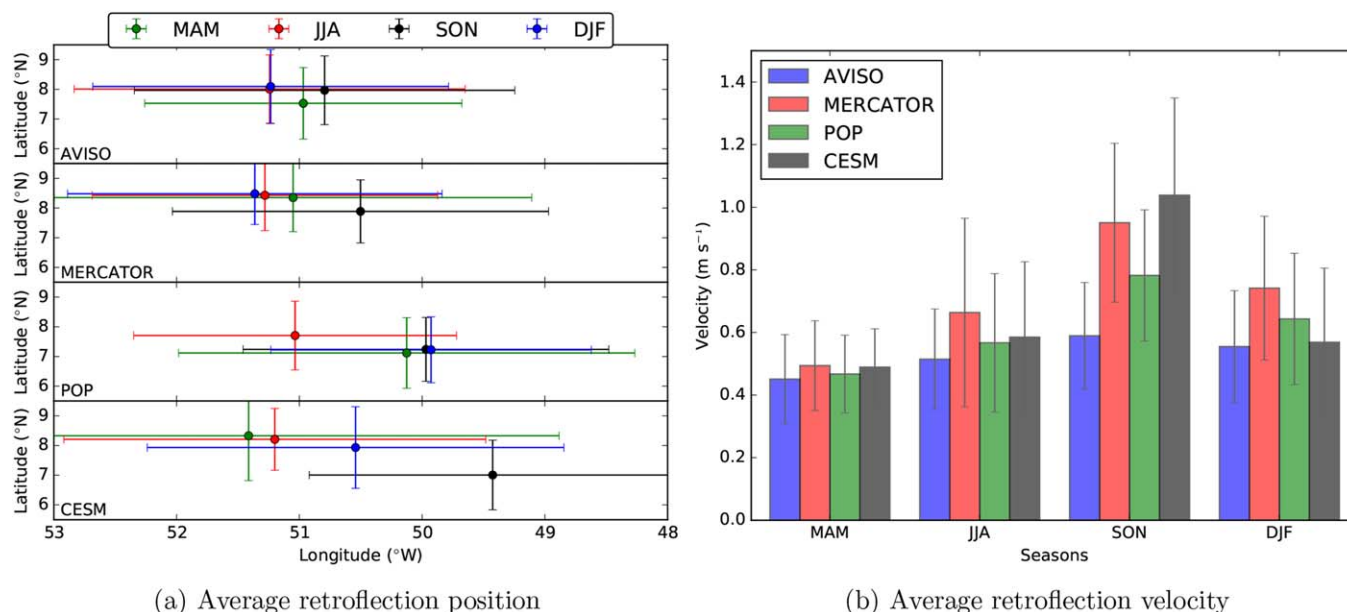


**Figure 4.** Annual cycle of the (a) average retroreflection position and the (b) retroreflection velocity, grouped by season. The retroreflection position and velocity are derived from weekly averaged SSH and velocity fields. The error bars in both figures are one standard deviation.

no clear seasonal variations for AVISO and Mercator (Figure 4a). In POP and CESM, there is slightly more seasonal variation in retroreflection position, in particular in longitude (POP) and latitude (CESM).

The meridional velocity ( $v_*$ ) is also determined near the point of retroreflection to investigate the seasonal cycle in the NBC retroreflection strength (Figure 4b). Although the position of this retroreflection point varies, its velocity shows a clear seasonal pattern in accordance with Table 2 and Johns et al. (1990). The retroreflection velocity is stronger in autumn (SON) compared to spring (MAM). Note that the error bars are smaller during spring due to the relative small abundance of the retroreflection (Table 2) in spring compared to the other seasons.

Among the different data sets, the annual average retroreflection velocity for Mercator and CESM is stronger compared to AVISO and POP. All data sets show similar velocities during December–July, while the results differ for the remaining months. During December–July, the NBC retroreflection region is (highly) variable and the retroreflection is relatively weak or absent, which contributes to the consistency among the data sets. For the other months, the difference between AVISO and Mercator could be due to an underestimation of the derived (geostrophic) velocities from SSH fields in AVISO, since SSH is only observed by AVISO. The difference between POP and CESM is related to the different (annual) average wind stress field near the NBC retroreflection, which is 19% stronger (spatial mean 40°W–60°W; 7°S–20°N) in CESM compared to POP.

The probability density function of the retroreflection position is shown in Figure 5. Qualitatively, the probability density functions of the four data sets overlap each other and are aligned along the continental shelf. The profiles are inclined by 123° (AVISO), 121° (Mercator), 123° (POP), and 120° (CESM) clockwise from the geographical north. The probability density function of POP and CESM display a double-peaked pattern, while AVISO and Mercator tend to a single-peaked pattern. The double-peaked pattern might be a model artifact or a seasonal effect (Figure 4a) in POP and CESM. Note that the available time series of POP and CESM are relatively short compared to AVISO and Mercator.

#### 4.2. Ring-Shedding Events

The retroreflection distance time series of AVISO shows a significant 44 and 56 day variability which is robust to the lag-window length (Table 3). The length of the retroreflection distance time series is restrained to  $N = 208$  weeks, the minimum continuous series available in all data sets (Table 1). Missing weeks (no retroreflection) were linearly interpolated to obtain a continuous time series. The significance of this variability is shown in Figure 6, using the Allen and Robertson (1996) test.

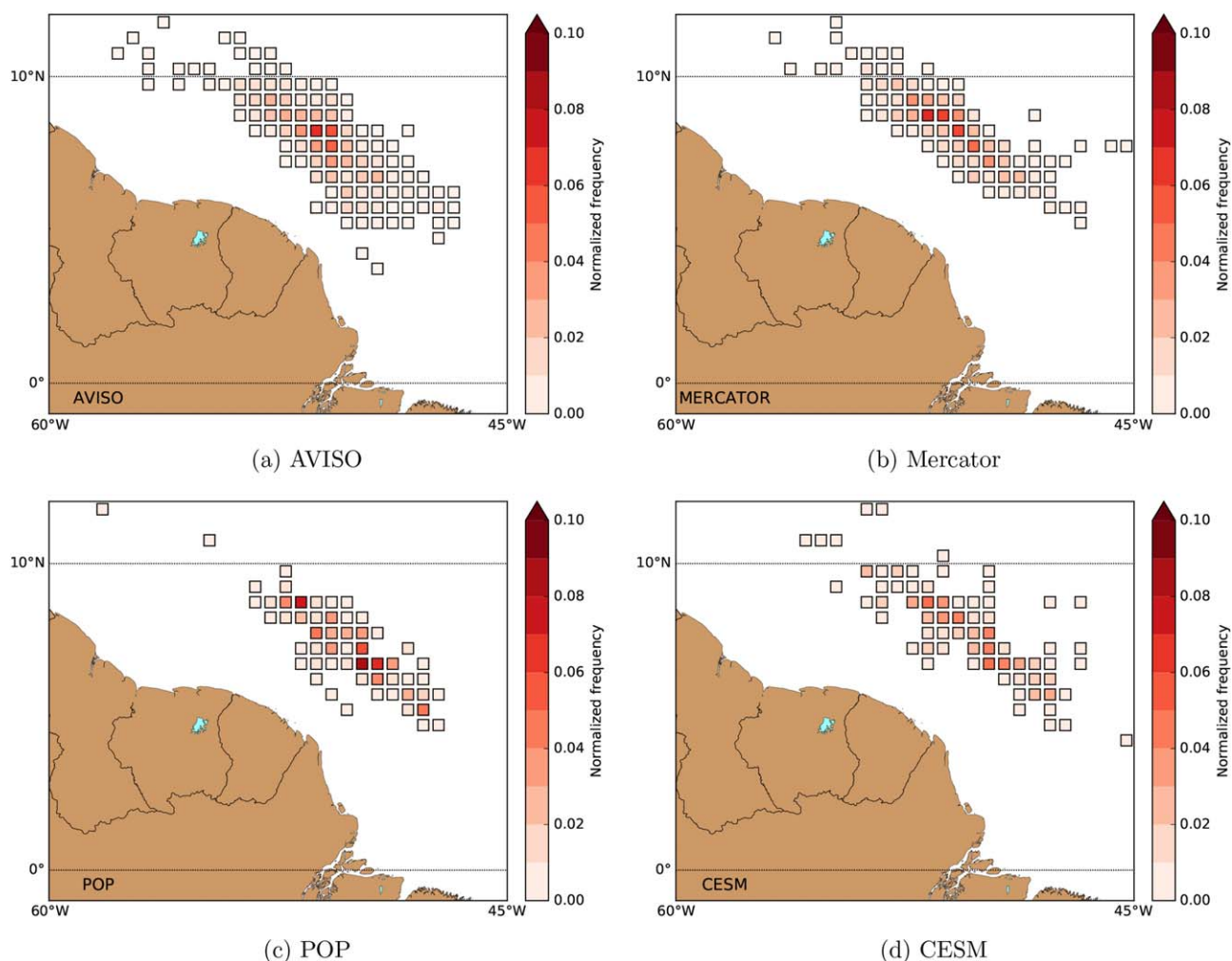


**Figure 5.** Probability density of the retroreflection position derived from weekly averaged SSH and velocity fields of (a) AVISO, (b) Mercator, (c) POP, and (d) CESM for the remaining 1,008, 427, 176, and 166 weeks, respectively. Note that the grid cells ( $0.5^\circ \times 0.5^\circ$ ) in the figures are not representative of the actual spatial resolution of the data sets.

However, the significance of this variability is strongly dependent on the selected range (14 October 2002 to 9 October 2006 in Figure 6) of the retroreflection distance time series. For example there is a period of about 10 years (1993–2000, 2007–2010) during which there are no significant frequencies in the retroreflection distance time series. The reason for this is the missing weeks due to the absence of the retroreflection (note that in total 139 weeks are missing over the full time series of 1,147 weeks, Table 2). The influence of missing weeks has been confirmed using surrogate time series in the form of a red noise process forced by a 49 day period. In this idealized case, significance (according to the (Allen & Robertson, 1996) test) is lost when several “gaps” are implemented. However, the variability is still significant in the noise basis. For the SSH data, we find that the PCs related to the 40 day period are significant in the noise basis during the 10 years of no significant frequencies. This indicates that the variability of ring shedding is not bound to certain periods, although the variability cannot always be distinguished in the data basis.

**Table 3**  
Significant Oscillations (95% Confidence Level) Determined From SSA of the Retroreflection Distance Time Series for Various Lag-Window Lengths (M)

Lag-window length <i>M</i> (weeks)	Period (days)			
	AVISO	Mercator	POP	CESM
25	-	-	-	-
50	44, 58	-	-	-
75	44, 55	39	-	-
100	42, 56	39, 58	-	-

Note. The total length is  $N = 208$  weeks.

For the SSH data, we find that the PCs related to the 40 day period are significant in the noise basis during the 10 years of no significant frequencies. This indicates that the variability of ring shedding is not bound to certain periods, although the variability cannot always be distinguished in the data basis.

In Mercator similar significant frequencies are found, a 39 and 58 day variability. Again, the significance of this result is sensitive to the selected range (14 October 2010 to 9 October 2014) and there are years (2007–2008, 2014–2016) with no significant frequencies. For

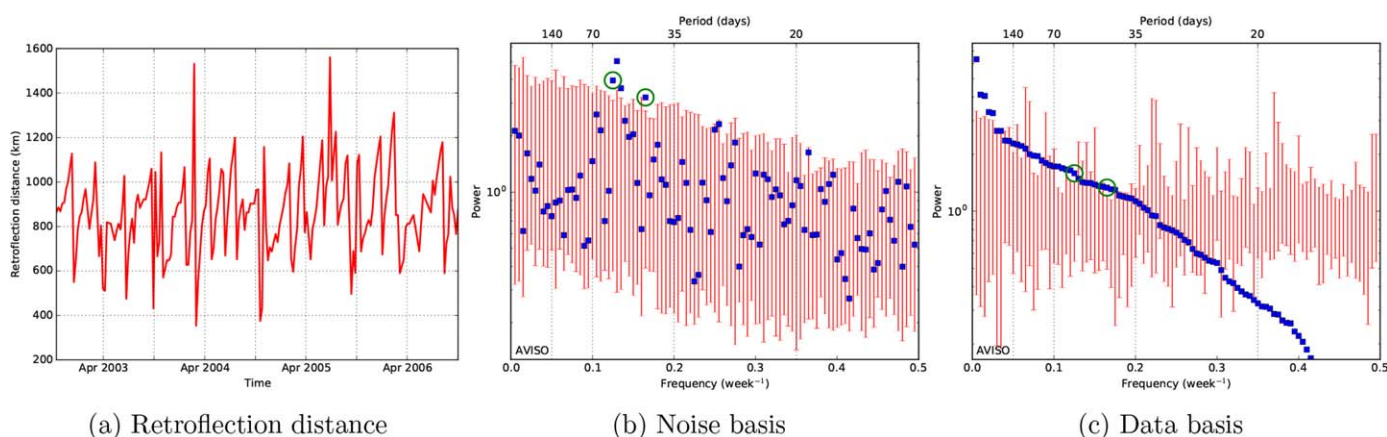


**Figure 6.** (a) Retroreflection distance time series during 14 October 2002 to 9 October 2006 of the AVISO data set. (b, c) The SSA conducted on the time series with the (b) red noise basis and (c) data basis for  $N = 208$  weeks, using a lag-window of  $M = 100$  weeks. The red vertical bars are the 95% confidence intervals and the blue data points correspond to a specific PC. The circled PCs are significant for both noise basis and data basis with an associated period of 42 and 56 days.

POP and CESM, there are no significant results in the retroreflection distance time series. For these data sets, is not possible to select a different time range, since both time series only have a length of 208 weeks. Similar to AVISO, POP displays a significant 44 day period only in the noise basis. In summary, the retroreflection distance time series analysis shows that there are only indications in AVISO and Mercator of a 40–60 day variability in the retraction of the NBC retroflection.

### 4.3. Variability in Sea Surface Height

This NBC variability as detected in the previous subsection will affect the SSH variability in the downstream regions of the NBC retroflection. Therefore, we define the NBC outflow region ( $45^{\circ}\text{W}–70^{\circ}\text{W}$  and  $3^{\circ}\text{N}–19^{\circ}\text{N}$ , black outlined region, Figure 7) to analyze the SSH variability in this region. The length of the time series is restricted to  $N = 208$  weeks, the minimum continuous series available in all data sets (Table 1). It appears that the results in M-SSA are not sensitive to the selected range of the time series for AVISO and Mercator. For consistency and comparison between AVISO and Mercator, we have analyzed the 208 weeks from April 2010 to April 2014 with M-SSA. In total, 46, 41, 48, and 42 PCs are retained during the prefiltering process

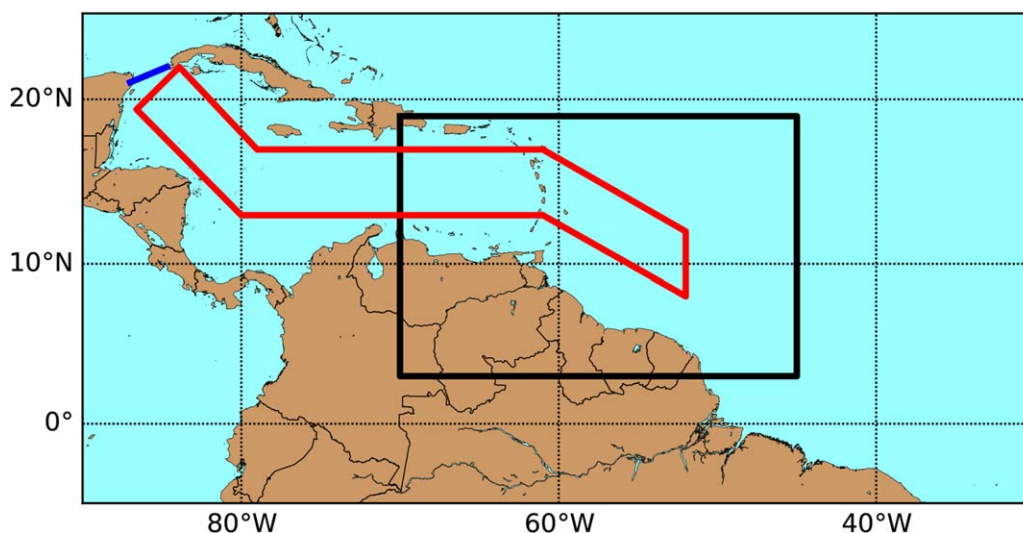


**Figure 7.** Two regions over which the SSH time series are analyzed. The black outlined region is the NBC outflow region and is used in Figure 8, over which M-SSA on SSH data is analyzed. The red outlined region is used in Figure 9 to study the propagation of sea level anomalies through the Lesser Antilles and in Figure 10, over which M-SSA on SSH data is analyzed. The blue section indicates the Yucatan Channel over which the (normal) velocity fields are analyzed and volume transport is determined.



**Table 4**  
Significant Oscillations (95% Confidence Level) Determined From M-SSA on the SSH Data Over the NBC Outflow Region (Black Outlined Region in Figure 7) for Various Lag-Window Lengths ( $M$ )

Lag-window length $M$ (weeks)	Period (days)			
	AVISO	Mercator	POP	CESM
25	41, 50, 59, 70	43, 51, 63, 70	44, 56, 70	50, 59, 70
50	44, 65	40, 47, 57, 70	40, 60, 70	43, 57, 70
75	43, 57, 67	44, 57, 67	40, 51, 59, 69	41, 52, 65
100	41, 51, 64	40, 47, 55, 62	44, 50, 59	44, 53, 61

Note. The total length is  $N = 208$  weeks.

for AVISO, Mercator, POP, and CESM, respectively. We find a significant 40–70 day variability for each data set (see Table 4) which is robust to the lag-window length. Note the resemblances of the results of the SSA (Table 3) and M-SSA (Table 4) analyses for AVISO. The 70 day variability is also found in a modeling study (Jouanno et al., 2009), where it is shown that this variability is related to NBC rings.

Using the appropriate ST-PC pairs (Plaut & Vautard, 1994), one can reconstruct the RCs (Ghil et al., 2002) to study the propagation of the SSH anomalies. If the variability (40–70 days) is associated with NBC rings, (north)westward propagating SSH anomalies are expected west of the NBC retroflection in the corresponding RCs. The propagation velocity of the anomalies is determined along the axis of maximum

amplitude of the anomalies. We have selected the first ST-PC pairs associated with the 43 day period for a lag-window of 50 weeks (see Table 4) to demonstrate the westward propagation of SSH anomalies. Hovmöller diagrams of the RCs for the four data sets are shown in Figure 8. There are westward propagating SSH anomalies in all the data sets. The anomalies propagate westward at a speed of  $16.6 \pm 1 \text{ km d}^{-1}$  (AVISO),  $17.0 \pm 1 \text{ km d}^{-1}$  (Mercator),  $15.1 \pm 1 \text{ km d}^{-1}$  (POP), and  $14.0 \pm 1 \text{ km d}^{-1}$  (CESM). Note the resemblance between the AVISO and Mercator results. The variance captured by the RCs is low ( $<3\%$ ), yet this

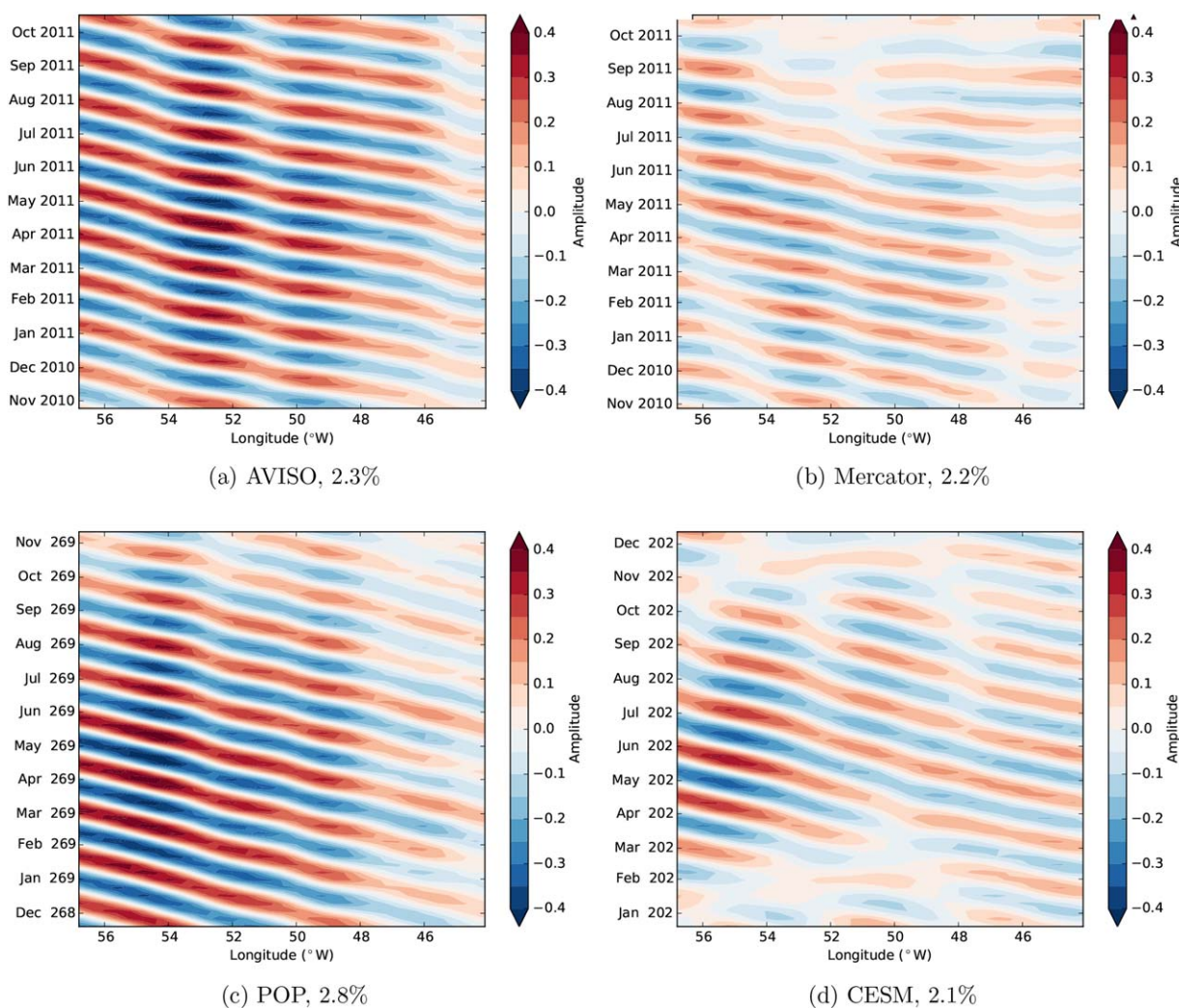


**Figure 8.** Hovmöller diagrams of the RCs (averaged over  $8^{\circ}\text{N}$ – $10^{\circ}\text{N}$ ) as a function of longitude and time. The (normalized) RCs are associated with the 43 day period, whereas the percentages indicate the variance of the corresponding RC pair for (a) AVISO, (b) Mercator, (c) POP, and (d) CESM.

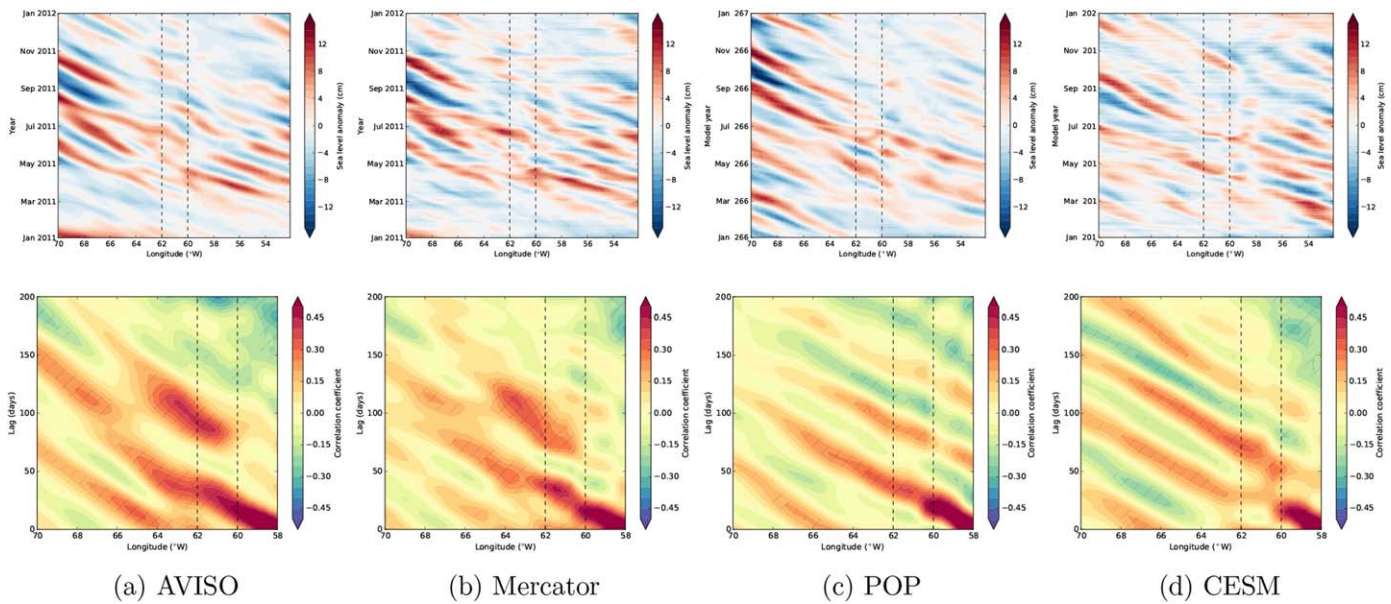


**Figure 9.** (top row) Hovmöller diagrams of SSH anomalies (averaged over latitude) along the red outlined region as presented in Figure 7 for four different data sets, displayed for a single year to emphasize the propagating character. The original time series are daily averaged SSH fields over 4 years. (bottom) Lagged correlation of the SSH anomalies with those at 58°W, where the hatched regions indicate a significant correlation at the 95% confidence level. In all figures, the dashed lines indicate the longitude of the island chain.

can be expected since a limited number of NBC rings are shed per year and NBC rings are local phenomena; M-SSA cannot distinguish between NBC rings and Rossby waves. It seems that the RCs are representing NBC rings, as the propagation speed is the same as reported in the literature, which is typically  $15 \pm 5 \text{ km d}^{-1}$  (Goni & Johns, 2001). The RCs associated with the 50–70 day variability show a similar westward propagation.

It is plausible that the variability originating from the NBC retroflection propagates with the background ocean flow (Alvera-Azcarate et al., 2009; Molinari et al., 1981), as shown in Figure 1, from the retroflection region via the Lesser Antilles into the Caribbean Sea (red outlined region, Figure 7). The 40–70 day variability is found in the NBC outflow region but it is possible that the SSH variability is not able to pass the Lesser Antilles. Therefore, we construct Hovmöller diagrams of SSH anomalies along the red outlined region in Figure 7 and study lagged correlations. The SSH anomalies are linearly detrended and a Butterworth high-pass filter (90 days) was applied to remove the annual cycle. The choice for the high-pass filter is to capture the propagation of eddies and is set to the approximate propagation time for eddies through the island chain. Besides, NBC rings can be positioned for a longer period near the island chain rather than advected immediately along or through the island chain. The sensitivity for the high-pass filter has been tested while applying a different range (50–180 days), which yields similar results.

Figure 9 (top row) shows these Hovmöller diagrams in SSH. From the diagrams it becomes clear that there is a westward propagation of SSH anomalies from the Atlantic Ocean into the Caribbean Sea. The anomalies are dampened around the island chain. This weakening of the SSH anomalies might be due to the interaction of the ocean (processes) with the bottom topography. For AVISO, it is also likely that there are large uncertainties in altimetry measurements in the region due to the presence of land. The SSH anomalies amplify after the island chain, due to the characteristic westward background flow. This result is also shown in Alvera-Azcarate et al. (2009, Figure 3). Note that their time series are not filtered and therefore show an annual cycle near the eastern entrance of the Caribbean basin. There is a resemblance in sea level anomalies in AVISO and Mercator for the year 2011.

**Table 5**  
*Significant Oscillations (95% Confidence Level) Determined From M-SSA on the SSH Data Over the Red Outlined Region in Figure 7 for Various Lag-Window Lengths (M)*

Lag-window length <i>M</i> (weeks)	Period (days)			
	AVISO	Mercator	POP	CESM
25	39, 56	39, 54, 63	55, 70	38
50	47, 54, 62, 70	39, 50, 57, 67	38, 48, 56, 70	38, 49, 59, 70
75	43, 51, 61	38, 46, 54, 67	40, 45, 69	45, 47, 65
100	42, 51, 59, 66	42, 49, 57	42, 49, 61	40, 47, 57, 64

Note. The total length is  $N = 208$  weeks.



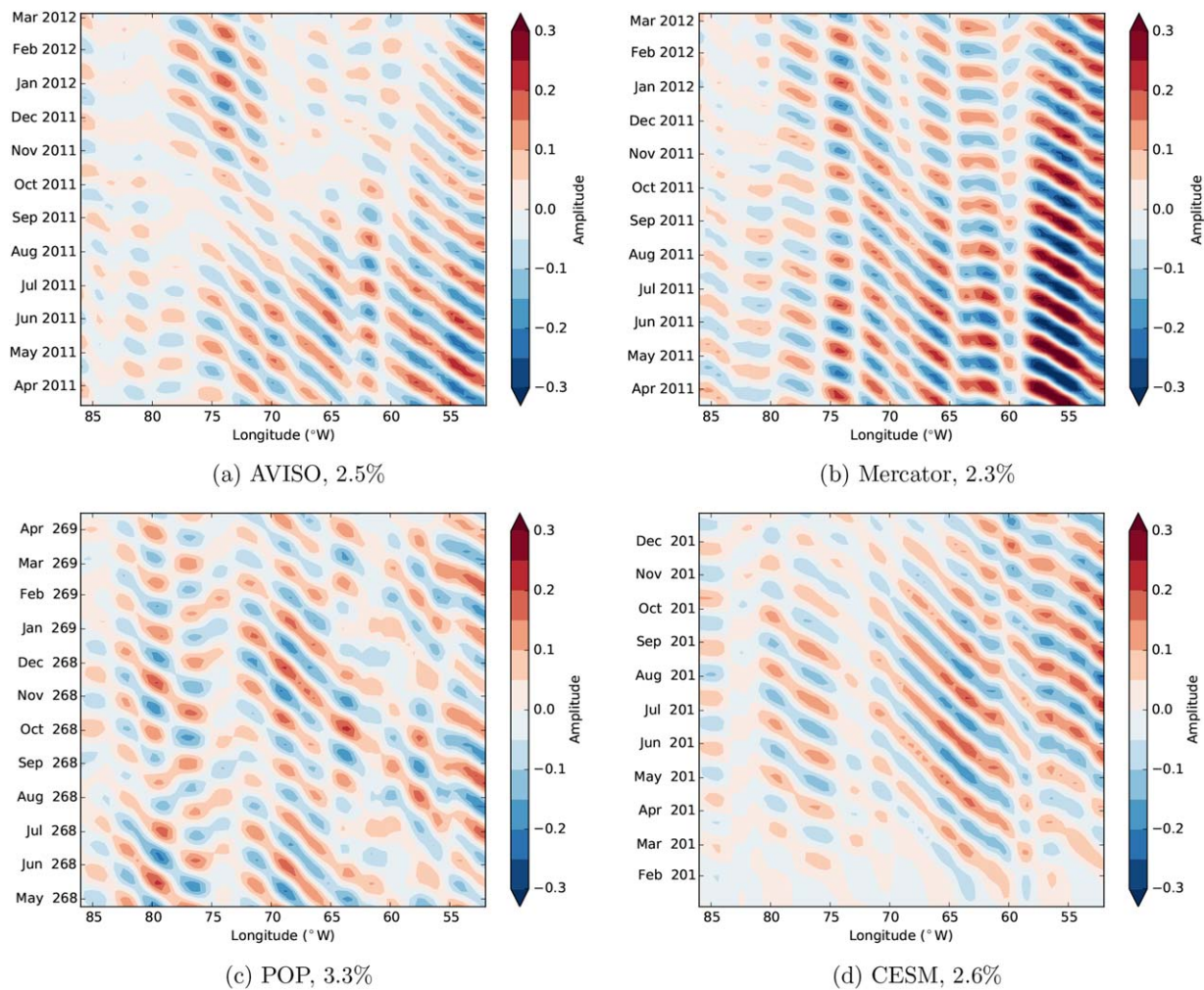


**Figure 10.** Hovmöller diagrams of the RCs (mean over latitude) along the red outlined region as presented in Figure 7. The (normalized) RCs are associated with the 43 day period, whereas the percentages indicate the variance of the corresponding RC pair for (a) AVISO, (b) Mercator, (c) POP, and (d) CESM.

In the lower row of Figure 9, lagged correlation of the SSH anomalies to 58°W are shown to demonstrate the propagation of SSH anomalies through the island chain. There are significant (95% confidence level) correlations in the Caribbean Sea, indicating that the variability in SSH has an Atlantic Ocean origin. All data sets show a significant lagged correlation at 66°W. AVISO even shows significant lagged correlation up to 70°W.

### 5. Results: Caribbean Analysis

In this section, the connection between the SSH variability in the Caribbean Sea and the variability in volume transport of the YC is analyzed.

#### 5.1. Variability in Sea Surface Height

Complete NBC rings and their filaments may act as a perturbation in the Caribbean basin, which in turn, produces eddies within the Caribbean Sea (Carton & Chao, 1999; Jouanno et al., 2009). Therefore, M-SSA is conducted over the red outlined region, indicated in Figure 7. The time series are prefiltered in a similar way as described in section 2 and in total 36, 34, 35, and 31 PCs are retained during the prefiltering

**Table 6**

Significant Oscillations (95% Confidence Level) Determined From M-SSA on the SSH Data Over the Entire Caribbean Sea, Including a 75–175 Day Band-Pass Filter, for Various Lag-Window Lengths (M)

Lag-window length M (weeks)	Period (days)			
	AVISO	Mercator	POP	CESM
25	123	-	-	-
50	124	117	131	-
75	125	117	125	110
100	127	-	109	117

Note. The total length is N = 208 weeks.

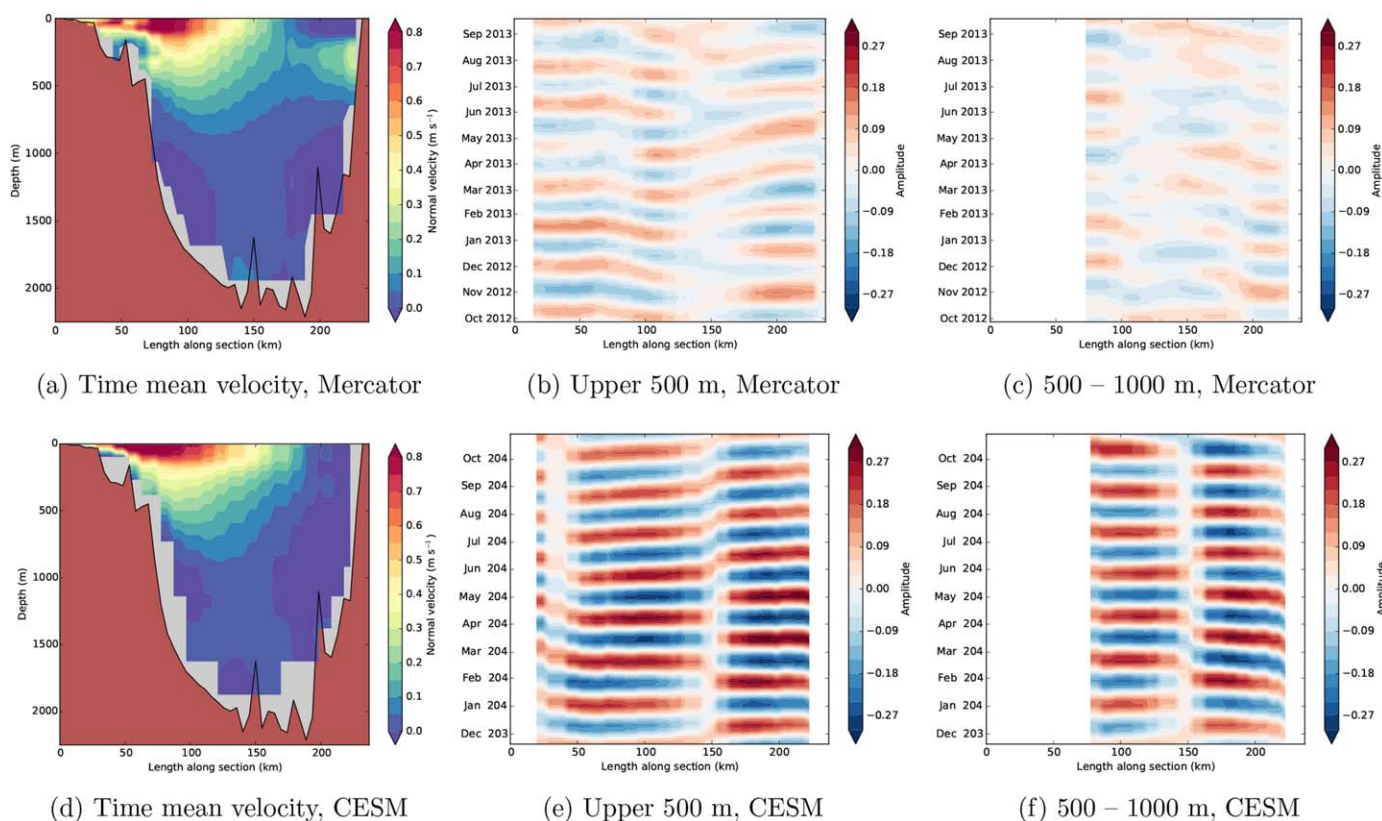


**Figure 11.** (a, d) Time mean velocity field in the Yucatan Channel over all available weekly averaged velocity fields, along the blue section as indicated in Figure 7. (b, e) The (normalized) RCs associated with the 48 day period, along the section and averaged over the upper 500 m. (c, f) The (normalized) RCs associated with the 48 day period, along the section and averaged over 500–1,000 m. The variance by this RC pair is 4.2% and 2.7% for Mercator and CESM, respectively.

process for AVISO, Mercator, POP, and CESM, respectively. The results are shown in Table 5 and indicate a significant 40–70 day variability.

To determine the propagation of the 40–70 day SSH variability, we determine RCs along the same region (Figure 7). The RCs associated with a 43 day period for a lag-window of 100 weeks (Table 5) show a westward propagation of SSH anomalies for all four data sets (see Figure 10). The Hovmöller diagrams indicate that SSH anomalies start in the Atlantic Ocean near the NBC retroflection (54°W) and enter the eastern entrance of the Caribbean Sea (63°W) and continue to propagate westward to the western exit (85°W). The SSH anomalies propagate westward with an average speed of  $12.1 \pm 1 \text{ km d}^{-1}$  (AVISO),  $11.4 \pm 1 \text{ km d}^{-1}$  (Mercator),  $11.0 \pm 1 \text{ km d}^{-1}$  (POP), and  $11.9 \pm 1 \text{ km d}^{-1}$  (CESM) between 63°W and 80°W. The RCs associated with the 50–70 day variability show a similar westward propagation. Near 60°W, the westward propagation is distorted, due to the effect of the Caribbean island chain.

**Table 7**

Significant Oscillations (95% Confidence Level) Determined From M-SSA on the Normal Velocity Fields in the Yucatan Channel Down to 1,000 m for Various Lag-Window Lengths (M)

Lag-window length <i>M</i> (weeks)	Period (days)	
	Mercator	CESM
25	47, 56	-
50	-	49, 70
75	38	69
100	38	-

Note. The total length is  $N = 208$  weeks.

The SSH variability in the Caribbean Sea is most likely following the background ocean flow in the Caribbean Sea (Alvera-Azcarate et al., 2009). Caribbean eddies are advected by the background current and can have maximum velocities of  $17 \text{ km d}^{-1}$  (Andrade & Barton, 2000), Murphy et al. (1999) and Carton and Chao (1999) find an average westward velocity of  $13 \pm 1$  and  $10 \pm 1 \text{ km d}^{-1}$ , respectively. Jouanno et al. (2009) report westward velocities of Caribbean eddies between 10 and  $13 \text{ km d}^{-1}$ . Near 80°W, the anomalies weaken and the westward propagation is distorted, which is likely the effect of the Nicaraguan Rise and is also shown in Alvera-Azcarate et al. (2009). This effect can also be seen in the SSH variance (see Figure 1a), where this quantity decreases at 80°W along the characteristic background ocean flow.



**Table 8**  
Significant Oscillations (95% Confidence Level) Determined From SSA on the Volume Transport in the Yucatan Channel for Various Lag-Window Lengths (*M*)

Lag-window length <i>M</i> (weeks)	Period (days)			
	Daily resolution		Weekly resolution	
	Mercator	CESM	Mercator	CESM
25	70	39, 50	39, 70	50
50	38, 41, 50, 58	39, 44, 47, 53, 58, 64	39	58, 64
75	38, 42, 66	40, 48, 53, 66, 70	66	46, 70
100	40, 48, 51, 58, 70	38, 46, 56, 67, 70	-	56

Note. The total length is  $N = 1,460$  days and  $N = 208$  weeks.

When M-SSA is conducted over the entire Caribbean Sea, while using weekly averaged SSH fields, also a significant 40–70 day variability over the entire Caribbean Sea (not shown here) is found for all four data sets. However, this variability is less robust compared to the variability found in the red outlined region. There is a significant spectral peak associated with the Rossby Whistle (Hughes et al., 2016), a basin resonant mode with a period of about 120 days, while applying M-SSA to the Caribbean Sea (Table 6). The SSH time series were filtered by a 75–175 day band-pass filter (the spectrum is mainly dominated by the 40–70 day variability), similar as in Hughes et al. (2016).

### 5.2. Variability in the Yucatan Channel

The variability in the YC is analyzed by applying M-SSA to the (normal) velocity fields (blue section in Figure 7) along a vertical section in the channel (cf., Figures 11a and 11d). The results from Mercator and CESM are the only two available data sets which have the daily horizontal velocity fields with depths down to the bottom (2,100 m) of the YC (see Table 1). We selected all the time series down to 1,000 m. The time series are prefiltered, but data reduction by PCA is not necessary since the total number of grid cells is relatively small compared to the previous SSH analyses. A 40–70 day variability is found for Mercator and CESM (Table 7) but is not robust to the lag-window length. Abascal et al. (2003) report from moorings similar variability (50–100 days) in the kinetic energy spectrum in the YC. There is no evidence for the Rossby Whistle, even while implementing a band-pass filter. Hughes et al. (2016) report that the signature of the Rossby Whistle for bottom pressure weakens in the Yucatan Basin and is even weaker in the Gulf of Mexico.

The RCs related to the 48 day period are shown in Figure 11 for Mercator and CESM. In Figure 11b and 11e, the profiles indicate a phase difference between the western and eastern part in the YC over the upper 500 m. This phase difference is also found between 500 and 1,000 m (Figures 11c and 11f) and is due to the fact (Ezer et al., 2003) that in the western (eastern) part of the YC, there is an outgoing (ingoing) volume transport (Figures 11a and 11d).

We also apply SSA to the net volume transport in the YC (i.e., Figure 2a). The time series has been filtered in a similar way as in Figure 2, a linear trend is removed and a Butterworth band-pass filter of 30–120 days is applied. Weekly averages show the same significant 40–70 day variability in YC transport (Table 8). Applying SSA to daily averages display additional significant periods in YC transport, due to the higher temporal resolution. The spectral peaks in Figure 2b that have a period of 40–70 days (Table 8) are significant in SSA. Abascal et al. (2003) report from moorings similar variability (20–40 days) in the volume mass transport in the YC, but part of this variability is filtered out by the band-pass filter. Note, however, that without the band-pass filter, none of the results are significant since the spectrum is dominated by low-frequency variability (>170 days; Ezer et al., 2003).

## 6. Summary, Discussion, and Conclusion

In this paper, we have studied the connection between the SSH variability in the NBC retroflection region and that in the Yucatan Channel volume transport, using four different data sets containing observed (AVISO), assimilated (Mercator), and model output (POP and CESM). We find a consistent 40–70 day SSH variability in the NBC retroflection region, propagating through the Caribbean Sea and connecting to the same frequency variability found in the velocity fields and volume transport in the YC.

The NBC retroflection is present in all data sets and the average position is  $50.9^\circ \pm 1.6^\circ\text{W}$  and  $7.9^\circ \pm 1.2^\circ\text{N}$ , which agrees well with earlier observed values (Condie, 1991; Csanady, 1985; Fratantoni & Glickson, 2002). The retroflection position often shows a southeastward retraction related to the shedding of NBC rings. The shedding has an approximate 40–60 day variability in AVISO and Mercator, confirming earlier results of the shedding of rings (Fratantoni et al., 1995; Johns et al., 1990). The retroflection distance time series is sensitive to the time period which is analyzed (nonstationary effects) which may explain the absence of this variability in POP and CESM.

The NBC retroflection affects the SSH variability in the downstream regions. All data sets show a clear 40–70 day variability for the NBC outflow region. Among the data sets, the reconstructed components show westward propagating SSH anomalies of approximately  $15 \text{ km d}^{-1}$ . Johns et al. (1990) also find this 40–60 day variability in the meridional velocity which is related to the shedding of NBC rings. A modeling study (Jouanno et al., 2009) shows that the 70 day variability is also related to NBC rings. Variability from the NBC is able to enter the Caribbean Sea, which has been demonstrated by other studies (Carton & Chao, 1999; Johns et al., 2002; Jouanno et al., 2009). The same 40–70 day variability in SSH is found in the Caribbean Sea. The reconstructed components associated with this variability show that it originates near the NBC retroflection and enters the eastern entrance of the Caribbean Sea. The average westward speed in the Caribbean Sea is  $12 \text{ km d}^{-1}$ , well within reported ranges (Andrade & Barton, 2000; Carton & Chao, 1999; Jouanno et al., 2009; Murphy et al., 1999). We also find some indications of the Rossby Whistle (Hughes et al., 2016).

As addressed by Jouanno et al. (2008, 2009), the variability found in the Caribbean Sea could be the effect of Rossby waves. They show that the first baroclinic Rossby wave has a 50–65 day period. The Rossby wave can act as a perturbation (similar to the filaments of the NBC rings) and generate eddies at the eastern entrance of the Caribbean Sea. It is therefore difficult to distinguish the SSH variability due to NBC rings and Rossby waves in the Caribbean Sea. On the other hand, M-SSA also shows a 40–50 day variability and, as demonstrated, this is related to variability found in the NBC. The 50–70 day variability could be a combination of both NBC rings and Rossby waves (Jouanno et al., 2009). Still, SSH anomalies due to both NBC rings and Rossby waves originate from an upstream region (i.e., the eastern entrance of the Caribbean Sea) and propagate toward the YC. As this variability is found in POP, which has only a seasonal mean atmospheric forcing, it is purely intrinsic (so not caused by variability in the atmospheric forcing).

Although we could not determine the YC volume transport variability for AVISO and POP, both Mercator and CESM output show the same significant 40–70 day variability in the YC volume transport. There is a phase difference between the eastern and western part in the YC, likely a signature of an eddy passing through the YC. Such a phase difference is also found by Ezer et al. (2003); the PC of their second EOF displays variability on 2 and 11 months time scales and influences the variability in the Loop Current.

Based on our analyses of the 40–70 day variability in the four data sets, we conclude that the physical mechanism of the short-term variability in the YC is related to the propagation of variability from upstream regions and originates from processes in the NBC retroflection region.

#### Acknowledgments

This work is part of the research program ALW-Caribbean with project 858.14.061 (SCENES), which is financed by the Netherlands Organisation for Scientific Research (NWO). The altimeter products were produced and distributed by AVISO (<https://www.aviso.altimetry.fr/en/data.html>). The Mercator data set was provided by Copernicus-Marine environment monitoring service (<http://marine.copernicus.eu/services-portfolio/access-to-products/>). The model output from POP and CESM used in this work are available upon request from the authors.

#### References

- Abascal, A., Sheinbaum, J., Candela, J., Ochoa, J., & Badan, A. (2003). Analysis of flow variability in the Yucatan Channel. *Journal of Geophysical Research: Oceans*, *108*(C12), 3381. <https://doi.org/10.1029/2003JC001922>
- Allen, M., & Robertson, A. (1996). Distinguishing modulated oscillations from coloured noise in multivariate datasets. *Climate Dynamics*, *12*(11), 775–784.
- Allen, M. R., & Smith, L. A. (1996). Monte Carlo SSA: Detecting irregular oscillations in the presence of colored noise. *Journal of Climate*, *9*(12), 3373–3404.
- Alvera-Azcarate, A., Barth, A., & Weisberg, R. H. (2009). The surface circulation of the Caribbean Sea and the Gulf of Mexico as inferred from satellite altimetry. *Journal of Physical Oceanography*, *39*(3), 640–657.
- Andrade, C. A., & Barton, E. D. (2000). Eddy development and motion in the Caribbean Sea. *Journal of Geophysical Research: Oceans*, *105*(C11), 26191–26201.
- Bunge, L., Ochoa, J., Badan, A., Candela, J., & Sheinbaum, J. (2002). Deep flows in the Yucatan Channel and their relation to changes in the Loop Current extension. *Journal of Geophysical Research: Oceans*, *107*(C12), 3233. <https://doi.org/10.1029/2001JC001256>
- Candela, J., Tanahara, S., Crepon, M., Barnier, B., & Sheinbaum, J. (2003). Yucatan Channel flow: Observations versus CLIPPER ATL6 and MERCATOR PAM models. *Journal of Geophysical Research: Oceans*, *108*(C12), 3385. <https://doi.org/10.1029/2003JC001961>
- Carton, J. A., & Chao, Y. (1999). Caribbean Sea eddies inferred from TOPEX/Poseidon altimetry and a 1/6 Atlantic Ocean model simulation. *Journal of Geophysical Research: Oceans*, *104*(C4), 7743–7752.
- Castelão, G., & Johns, W. (2011). Sea surface structure of North Brazil Current rings derived from shipboard and moored acoustic Doppler current profiler observations. *Journal of Geophysical Research: Oceans*, *116*, C01010. <https://doi.org/10.1029/2010JC006575>
- Cetina-Heredia, P., Roughan, M., Van Sebille, E., & Coleman, M. (2014). Long-term trends in the East Australian Current separation latitude and eddy driven transport. *Journal of Geophysical Research: Oceans*, *119*, 4351–4366. <https://doi.org/10.1002/2014JC010071>
- Chérubin, L., & Richardson, P. L. (2007). Caribbean current variability and the influence of the Amazon and Orinoco freshwater plumes. *Deep Sea Research Part I: Oceanographic Research Papers*, *54*(9), 1451–1473.
- Condie, S. A. (1991). Separation and recirculation of the North Brazil Current. *Journal of Marine Research*, *49*(1), 1–19.
- Csanady, G. (1985). A zero potential vorticity model of the north Brazilian coastal current. *Journal of Marine Research*, *43*(3), 553–579.
- Dencausse, G., Arhan, M., & Speich, S. (2010). Spatio-temporal characteristics of the Agulhas Current retroflection. *Deep Sea Research Part I: Oceanographic Research Papers*, *57*(11), 1392–1405.
- Ezer, T., Oey, L.-Y., Lee, H.-C., & Sturges, W. (2003). The variability of currents in the Yucatan Channel: Analysis of results from a numerical ocean model. *Journal of Geophysical Research: Oceans*, *108*(C1), 3012. <https://doi.org/10.1029/2002JC001509>

- Fratantoni, D. M., & Glickson, D. A. (2002). North Brazil Current ring generation and evolution observed with SeaWiFS. *Journal of Physical Oceanography*, *32*(3), 1058–1074.
- Fratantoni, D. M., Johns, W. E., & Townsend, T. L. (1995). Rings of the North Brazil Current: Their structure and behavior inferred from observations and a numerical simulation. *Journal of Geophysical Research: Oceans*, *100*(C6), 10633–10654.
- Fratantoni, D. M., & Richardson, P. L. (2006). The evolution and demise of North Brazil Current rings. *Journal of Physical Oceanography*, *36*(7), 1241–1264.
- Ghil, M., Allen, M. R., Dettinger, M. D., Ide, K., Kondrashov, D., Mann, M. E., et al. (2002). Advanced spectral methods for climatic time series. *Reviews of Geophysics*, *40*(1), 1003. <https://doi.org/10.1029/2000RG000092>
- Goni, G. J., & Johns, W. E. (2001). A census of North Brazil Current rings observed from TOPEX/POSEIDON altimetry: 1992–1998. *Geophysical Research Letters*, *28*(1), 1–4.
- Hallberg, R. (2013). Using a resolution function to regulate parameterizations of oceanic mesoscale eddy effects. *Ocean Modelling*, *72*, 92–103.
- Hughes, C. W., Williams, J., Hibbert, A., Boening, C., & Oram, J. (2016). A Rossby whistle: A resonant basin mode observed in the Caribbean Sea. *Geophysical Research Letters*, *43*, 7036–7043. <https://doi.org/10.1002/2016GL069573>
- Hurrell, J. W., Holland, M. M., Gent, P. R., Ghan, S., Kay, J. E., Kushner, P. J., et al. (2013). The community earth system model: A framework for collaborative research. *Bulletin of the American Meteorological Society*, *94*(9), 1339–1360.
- Johns, W. E., Lee, T. N., Schott, F. A., Zantopp, R. J., & Evans, R. H. (1990). The North Brazil Current retroflection: Seasonal structure and eddy variability. *Journal of Geophysical Research: Oceans*, *95*(C12), 22103–22120.
- Johns, W. E., Townsend, T. L., Fratantoni, D. M., & Wilson, W. D. (2002). On the Atlantic inflow to the Caribbean Sea. *Deep Sea Research Part I: Oceanographic Research Papers*, *49*(2), 211–243.
- Johns, W. E., Zantopp, R. J., & Goni, G. J. (2003). Cross-gyre transport by North Brazil Current rings. *Elsevier Oceanography Series*, *68*, 411–441.
- Jouanno, J., & Sheinbaum, J. (2013). Heat balance and eddies in the Caribbean upwelling system. *Journal of Physical Oceanography*, *43*(5), 1004–1014.
- Jouanno, J., Sheinbaum, J., Barnier, B., & Molines, J.-M. (2009). The mesoscale variability in the Caribbean Sea. Part II: Energy sources. *Ocean Modelling*, *26*(3), 226–239.
- Jouanno, J., Sheinbaum, J., Barnier, B., Molines, J.-M., Debreu, L., & Lemarié, F. (2008). The mesoscale variability in the Caribbean Sea. Part I: Simulations and characteristics with an embedded model. *Ocean Modelling*, *23*(3), 82–101.
- Le Bars, D., Durgadoo, J., Dijkstra, H., Biastoch, A., & De Ruijter, W. (2014). An observed 20-year time series of Agulhas leakage. *Ocean Science*, *10*(4), 601.
- Le Bars, D., Viebahn, J., & Dijkstra, H. (2016). A Southern Ocean mode of multidecadal variability. *Geophysical Research Letters*, *43*, 2102–2110. <https://doi.org/10.1002/2016GL068177>
- Lin, Y., Sheng, J., & Greatbatch, R. J. (2012). A numerical study of the circulation and monthly-to-seasonal variability in the Caribbean Sea: The role of Caribbean eddies. *Ocean Dynamics*, *62*(2), 193–211.
- Madec, G., & The NEMO Team. (2008). NEMO ocean engine. *Note du Pôle de modélisation, Institut Pierre-Simon Laplace (IPSL), France*. *27*, 1288–1619.
- Molinari, R. L., Spillane, Brooks, M., Atwood, I. D., & Duckett, C. (1981). Surface currents in the Caribbean Sea as deduced from Lagrangian observations. *Journal of Geophysical Research: Oceans*, *86*(C7), 6537–6542.
- Murphy, S. J., Hurlburt, H. E., & O'Brien, J. J. (1999). The connectivity of eddy variability in the Caribbean Sea, the Gulf of Mexico, and the Atlantic Ocean. *Journal of Geophysical Research: Oceans*, *104*(C1), 1431–1453.
- Ochoa, J., Sheinbaum, J., Badan, A., Candela, J., & Wilson, D. (2001). Geostrophy via potential vorticity inversion in the Yucatan Channel. *Journal of Marine Research*, *59*(5), 725–747.
- Oey, L.-Y. (2004). Vorticity flux through the Yucatan Channel and Loop Current variability in the Gulf of Mexico. *Journal of Geophysical Research: Oceans*, *109*, C10004. <https://doi.org/10.1029/2004JC002400>
- Plaut, G., & Vautard, R. (1994). Spells of low-frequency oscillations and weather regimes in the Northern Hemisphere. *Journal of the Atmospheric Sciences*, *51*(2), 210–236.
- Richardson, P. L. (2005). Caribbean Current and eddies as observed by surface drifters. *Deep Sea Research Part II: Topical Studies in Oceanography*, *52*(3), 429–463.
- Schmeits, M. J., & Dijkstra, H. A. (2000). Physics of the 9-month variability in the Gulf Stream region: Combining data and dynamical systems analyses. *Journal of Physical Oceanography*, *30*(8), 1967–1987.
- Schmitz, W. J., & Richardson, P. L. (1991). On the sources of the Florida Current. *Deep Sea Research Part A. Oceanographic Research Papers*, *38*, S379–S409.
- Sheinbaum, J., Candela, Badan, J. A., & Ochoa, J. (2002). Flow structure and transport in the Yucatan Channel. *Geophysical Research Letters*, *29*(3). <https://doi.org/10.1029/2001GL013990>
- Simmons, H. L., & Nof, D. (2002). The squeezing of eddies through gaps. *Journal of Physical Oceanography*, *32*(1), 314–335.
- Smith, R., Jones, P. W., Briegleb, B., Bryan, F., Danabasoglu, G., Dennis, J., et al. (2010). *The Parallel Ocean Program (POP) reference manual: Ocean component of the Community Climate System Model (CCSM) and Community Earth System Model (CESM)* (Rep. LAUR-01853, Vol. 141, pp. 1–140).
- van Westen, R. M., & Dijkstra, H. A. (2017). Southern Ocean origin of multidecadal variability in the North Brazil Current. *Geophysical Research Letters*, *40*, 10540–10548. <https://doi.org/10.1002/2017GL074815>
- Vautard, R., & Ghil, M. (1989). Singular spectrum analysis in nonlinear dynamics, with applications to paleoclimatic time series. *Physica D: Nonlinear Phenomena*, *35*(3), 395–424.
- Weijer, W., Maltrud, M., Hecht, M. W., Dijkstra, H. A., & Klihuis, M. A. (2012). Response of the Atlantic Ocean circulation to Greenland Ice Sheet melting in a strongly-eddy ocean model. *Geophysical Research Letters*, *39*, L09606. <https://doi.org/10.1029/2012GL051611>